Supporting Information

Virtual Melting: A New Mechanism of Stress Relaxation Under High Strain Rate Loading

Valery I. Levitas[a] and Ramon Ravelo[b]

[a] *Iowa State University, Departments of Aerospace Engineering, Mechanical Engineering, and Material Science and Engineering, Ames, Iowa 50011, USA;*

[b] *Physics Department and Materials Research Institute, University of Texas, El Paso, TX 79968 and Computational Physics Division, Los Alamos National Laboratory, Los Alamos, NM 87545*

1. Methods of Advanced Thermodynamic Calculations

Since melting is considered the only dissipative process, the thermodynamic driving force per unit unloaded volume for the melting for isothermal loading is equal to the total dissipation [1, 2]:

$$X_m = W + \Delta s(T - T_m(0))) + (\psi_c^h(\varepsilon^*) - \psi_m^h(\varepsilon^m)) + \psi_c^{dev}(\varepsilon^*). \tag{1}$$

Here, $W = \int_{\varepsilon^*}^{\varepsilon^m} \sigma_1(\varepsilon)d\varepsilon$ is the the transformation work, which takes into account the actual stress-strain curve $\sigma_1(\varepsilon)$ during the melting; ψ^h and ψ^{dev} are the elastic energy of hydrostatic and deviatoric stresses (strains); Δs is the jump in entropy; T is the temperature at which the melting is started (at $\varepsilon = \varepsilon^*$); $T_m(0)$ is the thermodynamic melting temperature for stress-free solid; and subscripts c and m are for crystalline and molten states, respectively.

Let $p_c(\varepsilon)$ and $p_m(\varepsilon)$ be the equations of state of the crystalline and molten phases (Fig. 1). The equation of state for melt starts at point ($\varepsilon = \varepsilon_0$ and $\sigma_1 = 0$), where $\varepsilon_0 < 0$ is the volumetric transformation strain at melting at pressure $p = 0$. Then,

$$\psi_c^h(\varepsilon^*) = \int_0^{\varepsilon^*} p_c d\varepsilon; \quad \psi_c^{dev}(\varepsilon^*) + \psi_c^h(\varepsilon^*) = \int_0^{\varepsilon^*} \sigma_1 d\varepsilon; \quad \psi_m^h(\varepsilon^m) = \int_{\varepsilon_0}^{\varepsilon_m} p_m d\varepsilon, \tag{2}$$

and

$$X_m = \int_0^{\varepsilon^m} \sigma_1 d\varepsilon - \int_{\varepsilon_0}^{\varepsilon_m} p_m d\varepsilon + \Delta s(T - T_m(0)). \tag{3}$$

Geometrically, the mechanical driving force for melting is equal to the difference between the areas under the stress-strain curve for $\sigma_1(\varepsilon)$ $\{Oabc\varepsilon^m\}$ and for $p_m(\varepsilon)$ $\{\varepsilon_0 c\varepsilon^m\}$ (Fig. 1). For melting under constant temperature and hydrostatic pressure $p = \sigma_1$, the condition for thermodynamic equilibrium is

$$X^h = \sigma_1(\varepsilon_m - \bar{\varepsilon}) + \Delta s(T_m(\sigma_1) - T_m(0)) + (\psi_c^h(\bar{\varepsilon}) - \psi_m^h(\varepsilon_m)) = 0, \tag{4}$$

where $T_m(\sigma_1)$ is the equilibrium melting temperature under hydrostatic pressure $p = \sigma_1$, $\bar{\varepsilon} = \varepsilon_c(\sigma_1)$, $\varepsilon_c(p)$ and $\varepsilon_m(p)$ are the inverse equations of state for crystal and melt. The magnitude of the negative mechanical part of X_h is $\{O\varepsilon_0 cd\}$ (Fig. 1). It follows from Eq. (4):

$$T_m(\sigma_1) = T_m(0) + \left(\sigma_1(\bar{\varepsilon} - \varepsilon_m) - (\psi_c^h(\bar{\varepsilon}) - \psi_m^h(\varepsilon_m))\right)/\Delta s. \tag{5}$$

Expressing $\Delta s T_m(0)$ from Eq. (4) and substituting it in Eq. (1), we obtain

$$X_m = W + \sigma_1(\bar{\varepsilon} - \varepsilon_m) + \Delta s(T - T_m(\sigma_1)) + (\psi_c^h(\varepsilon^*) - \psi_c^h(\bar{\varepsilon})) + \psi_c^{dev}(\varepsilon^*). \tag{6}$$

Then, the condition $X_m = 0$ results in

$$T_m^{nh} = T_m(\sigma_1) - \left(\psi_c^{dev}(\varepsilon^*) + W + \sigma_1(\bar{\varepsilon} - \varepsilon^m) - (\psi_c^h(\bar{\varepsilon}) - \psi_c^h(\varepsilon^*))\right)/\Delta s =$$
$$T_m(\sigma_1) - \left(\int_0^{\varepsilon^m} \sigma_1 d\varepsilon - \int_0^{\bar{\varepsilon}} p_c d\varepsilon + \sigma_1(\bar{\varepsilon} - \varepsilon^m)\right)/\Delta s. \tag{7}$$

Geometrically, additional driving force for melting due to nonhydrostatic loading (the term in parentheses in Eq. (7)) is equal to the difference between the areas under the stress-strain curve $\sigma_1(\varepsilon)$ $\{Oabcd\}$ and the equation of state $p_c(\varepsilon)$ for crystal $\{Od\}$. All parameters for melting of Cu and Al for loading in the <110> direction and for Cu loading in the <111> direction are given in Table 1S.

Table 1S. Parameters for crystal loading (ε^*, ε^m, $\bar{\varepsilon}$, and σ_1^{m}, see Figs. 1 and 4S), maximum strain rate $\dot{\varepsilon}_{\max}$, initial T^* and final T_f temperatures, as well as melting temperature under hydrostatic conditions $T_m(\sigma_1^{\mathrm{m}})$ and decrease in melting temperature due to nonhydrostatic loading ΔT_m.

	ε^*	ε^m	$\bar{\varepsilon}$	$\dot{\varepsilon}_{\max}$	σ_1^{m}	T^*	T_f	$T_m(\sigma_1^{\mathrm{m}})$	ΔT_m
				ps^{-1}	GPa	K	K	K	K
Cu <110>	0.214	0.324	0.351	2.48	179.1	325	3084	5087	10074
Cu <111>	0.297	0.360	0.369	4.3	204.9	300	300	5434	9197
Cu <111>	0.301	0.353	0.375	3.97	215.1	197	2604	5565	8022
Al <110>	0.227	0.356	0.386	3.87	98.17	305	2711	3544	9945

Table 2S. Parameters in Murnaghan's (8) and Simon's (11) equations in Supplementary Materials.

	p_0	b	T_0	α	β
	GPa		K	GPa	
Cu	39.096	3.98	1327	15.3691	0.529458
Al	33.576	2.81	324	2.56529	0.647822

Table 3S. Parameters in Eq.(14) in Supplementary Materials for the reduction in melting temperature due to nonhydrostatic loading.

	T_f	A_σ	B_σ	C_σ	A_ε	B_ε	C_ε
	K	K	K/GPa	K/GPa^2	K	K	K
Cu <110>	3084	-1128	44.67	0.1008	4174	-82665	517956
Cu <111>	300	-1845	64.52	0.0518	-2182	20997	59602
Cu <111>	2604	-1137	42.24	0.0020	-299	-2684	101753
Al <110>	2711	-441	15.26	0.9295	5162	-96069	493689

The Murnaghan's equation of state for crystal, $p_c(\varepsilon)$, its inverse form, and the corresponding expressions for ψ_c^h and ψ_c^{dev} are:

$$p_c = p_0((1-\varepsilon)^{-b} - 1); \quad \varepsilon = 1 - \left(1 + \frac{p_c}{p_0}\right)^{-1/b}, \tag{8}$$

$$\psi_c^h = \int_0^{\varepsilon} p d\varepsilon = \frac{p_0}{b-1}\left((1-\varepsilon)^{b-1} - \varepsilon(b-1) - 1\right), \quad \psi_c^{dev} = \int_0^{\varepsilon^*} \sigma_1 d\varepsilon - \psi_c^h(\varepsilon^*), \tag{9}$$

where parameters p_0 and b for Cu and Al are given in Table 2S.

The jump in entropy Δs versus pressure p along the melting line $T_m(p)$ is found using the Clausius-Clapeyron relation

$$\Delta s = -\varepsilon_v / (dT_m(p)/dp), \tag{10}$$

where ε_v is the volumetric strain during the melting under the pressure (equal to ε_0 for $p = 0$). Since we consider cubic crystals with isotropic thermal expansion, the effect of deviatoric stresses on entropy will be neglected. The melting temperature versus pressure is found according to the Simon equation:

$$T_m = T_0(1 + p/\alpha)^{\beta}, \tag{11}$$

with parameters T_0, α, and β given in Table 2S for Cu and Al. The volume change during the melting $\varepsilon_v < 0$ along the melting line was calculated using MD simulations at constant temperature and pressure and approximated by the functions

$$|\varepsilon_v| = 0.008915 + 0.95820/p - 4.4612/p^2 \tag{12}$$

for Al and

$$|\varepsilon_v| = 0.013712 + 1.14436/p - 19.3125/p^2 + 105.80245/p^3 \tag{13}$$

for Cu. Substitution of Eqs. (11), (12), or (13) in Eq. (10) gives us jump in entropy. Functions $|\varepsilon_v|$ and Δs vs. pressure are shown in Figs. 1S and 2S for Cu and Al, respectively. While the

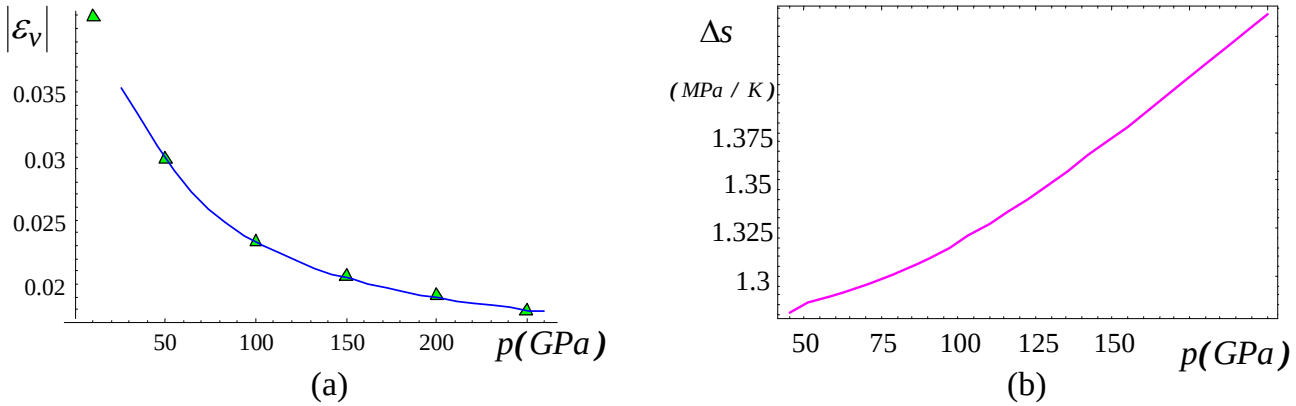

Figure 1S. (a) Jump in volumetric strain vs. pressure calculated using MD constant pressure and temperature simulations for Cu. (b) Jump in entropy during melting vs. pressure calculated using Clausius-Clapeyron equation (10) for Cu.

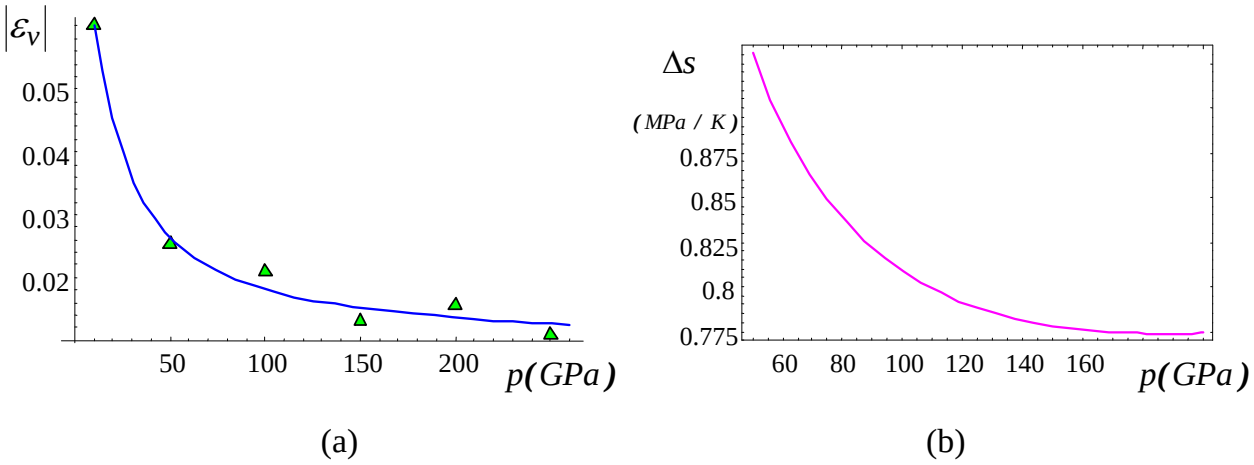

Figure 2S. (a) Jump in volumetric strain vs. pressure calculated using MD constant pressure and temperature simulations for Al. (b) Jump in entropy during melting vs. pressure calculated using Clausius-Clapeyron equation (10) for Al.

pressure dependence of Δs is very weak, it is interesting to note that it has different slopes for Cu and Al.

To calculate the melting temperature decrease for lower strains ε^* and corresponding stress $\sigma_1(\varepsilon^*)$, one needs to know the stress-strain curve $\sigma_1(\varepsilon)$ for elastic uniaxial loading (we will take it from Fig. 1, but it can be found phenomenologically if pressure dependence of elastic constants is known), the equation of state for solid $p(\varepsilon_c)$, and the stress strain curve $\sigma_1(\varepsilon)$ during melting, which has to be determined by MD simulation for each ε^* separately. To avoid additional MD simulations, we take into account that the reduction in σ_1 during the melting (line *abc* in Fig. 1) results in multiplication of work under constant stress $\sigma_1(\bar{\varepsilon} - \varepsilon^*)$ by a factor $h = 0.8831$ for Al (or $h = 0.8847$ for Cu) for <110> loading, which we used for all smaller ε^*. For <111> loading of Cu, we obtain $h = 0.9504$ for $T_f = 300K$ and $h = 0.8311$ for $T_f = 2604K$. The calculated melting temperature decrease (Eq. (7)) for lower strains ε^* and corresponding stress $\sigma_1(\varepsilon^*)$ can be approximated in the form

$$\Delta T_m = T_m(\sigma_1) - T_m^{nh}(\sigma_1) = A_\sigma + B_\sigma \sigma_1 + C_\sigma \sigma_1^2 = A_\varepsilon + B_\varepsilon \varepsilon^* + C_\varepsilon \varepsilon^{*2}, \tag{14}$$

where all constants are listed in Table 3S.

2. Methods of Molecular Dynamics Simulations

We performed multi-million atom non-equilibrium molecular dynamics (NEMD) simulations of shock wave compression, as well as smaller, Hugoniostat, and molecular dynamics (MD) simulations of quasi-isentropic compression to explored the dynamical evolution of the shocked state as a function of shock compression and crystallographic direction. The NEMD simulations comprised up to 12 million atoms arranged in a rectangular slab with periodic boundary conditions in the transverse directions. We employed the high-performance parallel molecular dynamics code

SPaSM [3] for the multi-million NEMD simulations. The procedure used to initiate a shock wave of a given strength is detailed in Ref. [4]: the crystal impacts an infinitely massive piston with a velocity $-u_p$, which produces a shock wave that propagates away from the piston with velocity $u_s - u_p$, u_s being the shock velocity. The NEMD sampled time scales were nominally of the order of 20-40 ps.

These simulations were augmented by constant-stress Hugoniostat simulations comprising 10^5 atoms arranged approximately in a cube. Details of the method can be found in Ref. [5]. We also carried out quasi-isentropic compression simulations, in which the system was uniaxially and homogeneously compressed to a final uniaxial strain using a specified time-profile for the strain-rate. Details of this method are given in [6].

The systems we chose to study were copper and aluminum single crystals shocked or quasi-isentropically compressed along the <110> direction and aluminum single crystal along the $\langle 111 \rangle$ direction. These crystallographic directions are known to produce large shear stresses with strain. The atomic interactions in the Cu and Al simulations were described using the well-tested embedded-atom method (EAM) models for Cu [7] and Al [8].

3. Results of additional MD simulations

1. The role of high shear stresses on the lowering of the melt temperature can be studied in greater detail via quasi-isentropic compression simulations, where the final compressive strain can be fixed, while the uniaxial strain-rate is varied. Using these types of simulations, we carried out a systematic study of virtual melting in both single and defective Cu crystals. We employed approximately cubic samples with 1.2×10^5 to 1.5×10^6 atoms and periodic boundary conditions. The final strain was fixed, and the strain rate was varied over 3 decades (from 2.5×10^9 to 2.5×10^{12} s^{-1}). As shown in Fig. 4 for Cu, along <110>, the shear stress increases rapidly with

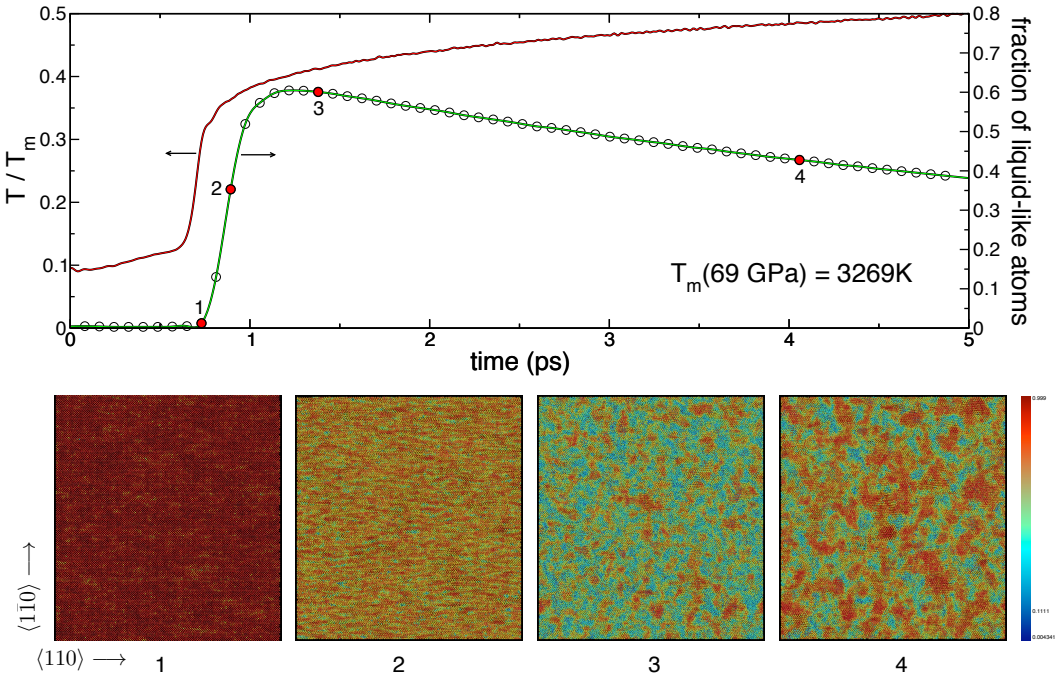

Figure 3S. 1.35-million-atom simulation of Cu quasi-isentropically compressed along <110> at an average strain rate of 2.5×10^{11} s^{-1} to a final strain of 0.20. The temperature profile (upper line) has been normalized by the equilibrium melt temperature at the final pressure (69 GPa). The fraction of liquid-like atoms (lower line) was computed from the order parameter q_6. The atomic profiles numbered at the bottom corresponds to the times numbered along the path. Atoms are colored according to q_6: solid (red) and liquid (blue).

compression. Under quasi-isentropic compression and at sufficiently high strain rates, we find that the system can melt at $T \simeq 0.35 T_m(p)$ (Fig. 3S). Figure 3S also shows a sequence of snapshots of the atomic configurations in a 1.35-million-atom single crystal Cu simulation in which the system was quasi-isentropically compressed along the <110> orientation at an average strain rate of 2.5×10^{11} s^{-1} to a final strain of 0.20. Also shown is the temperature (red line) normalized by the equilibrium melt temperature at the equilibrium pressure (69 GPa). The fraction of liquid atoms (green line) as a function of time was computed by following the evolution of the local order parameter q_6 and evaluating the fraction of atoms with a value less than 0.6. It takes about 0.8 ps to compress the sample to strain of 0.20 at $\dot{\varepsilon} = 0.25$ ps^{-1}. At the point labeled 1 in Fig. 3S, the atoms are still in an elastic and uniaxially compressed state, with a very high elastic energy corresponding to the highest shear stress (45 GPa) along the path. From point 1 to point 3, the system transforms from uniaxially compressed elastic solid to an isotropic state due to virtual melting. The virtual melting is partial at this strain and strain rate, and the liquid regions (blue atoms) coarsened rapidly. At the point labeled 3, the material is more isotropic, the elastic energy has been reduced significantly, and the temperature has increased due to the enthalpy difference between the isotropic liquid and the uniaxially compressed elastic solid. The time scale for this conversion is less than 1 ps. The decrease of the fraction of liquid atoms with time is caused by re-solidification from the melt (red atoms, point 4 along the path) followed by further reduction in the shear stress and an increase in temperature. From the enthalpy differences between the uniaxially compressed solid, supercooled liquid, and isotropic solid, the temperature profile as a function of time can be evaluated with excellent agreement with the simulations.

2. In addition, crystallization kinetics unambiguously suggests that the disordering represents the virtual melt rather than amorphization. Increase in temperature increases thermal fluctuations and promotes kinetics of crystallization from both melt and glass. However, the driving

force for crystallization of the melt and glass is the increasing function of $T_m - T$ and $T - T_g > 0$, respectively (where T_g is the glass transition temperature); thus temperature has opposite effect on these driving forces. We assume that T_g is below temperature at the end of our calculations, otherwise, there is no sense to talk about the crystallization of glass. For glass, the driving force for crystallization increases with temperature growth and crystallization rate has to be faster with increasing temperature. For melt, the driving force reduces with temperature increase and (if thermodynamic effect exceeds the kinetic one) crystallization rate may decrease with growing temperature. Since in all our MD simulations the crystallization rate decreased with the growing temperature, we can conclude that the disordered state is the virtual melt rather than glass.

3. For strain rate smaller than some threshold, melting occurs heterogeneously rather than in the entire volume (Fig. 3S). The volume fraction of disordered regions decreases with the decrease in strain rate. Note that if the remaining crystals are surrounded by melt and are under hydrostatic conditions, the total energy will be smaller than for complete melting, and the driving force will be even larger. This is because the energy of hydrostatically loaded crystal is much smaller than the energy of the melt below melting temperature. Crystallization time drastically depends on the existence of residual crystalline clusters, which can serve as nucleation cites. The higher are the shock strength (or strain rate) and temperature, the less probability there is of finding residual crystalline clusters in melt. Much more time is required for homogeneous nucleation of the crystal phase.

4. Fig. 4S shows the stresses and temperature evolution, and prescribed strain rate vs. uniaxial strain obtained using MD simulations for <110> shock loading of Al, similar to Fig. 1 for Cu. A well-tested EAM potential for Cu [8] was used.

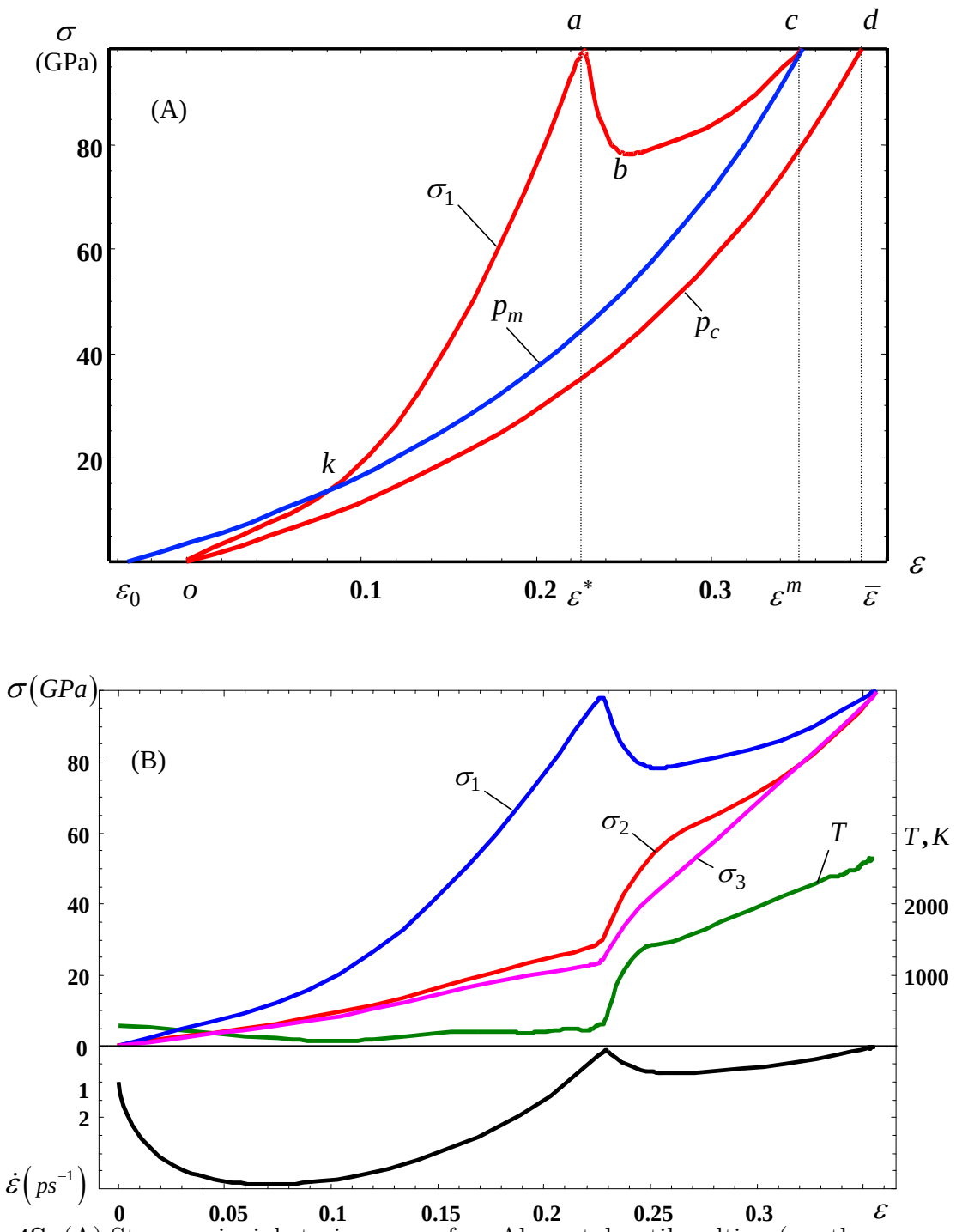

Figure 4S. (A) Stress-uniaxial strain curve of an Al crystal until melting (σ_1, the same as in Fig. 4S, B) and equations of state of molten (p_m) and crystalline (p_c) phases. Area between curves $\{Oabcd\}$ and $\{Od\}$ is the additional driving force for melting due to nonhydrostatic loading. (B) Variation of normal stresses σ_i, temperature, and prescribed strain rate vs. uniaxial strain obtained using MD simulations for <110> shock loading of Al.

5. Supporting movie

Cu single crystal compressed quasi-isentropically along the <111> direction (out of plane) at a strain rate of $3 \times 10^{11} s^{-1}$ to a final uniaxial strain of 33% (σ_1=174 GPa) is shown. Axis x is along the $<1\bar{1}0>$ direction and axis y is along the $<11\bar{2}>$ direction. The cross section of atomic configuration in the left panel is 10 nm $\times$ 10 nm. Only atoms within a 1.7 nm thick slice are shown for clarity. Atoms are colored according to q_6 [9, 10] (red atoms are solid, green atoms are liquid). The right panel shows the time evolution of the temperature (normalized by the equilibrium melt temperature at the corresponding pressure), pressure (p) and shear stress (τ).

References

[1] Levitas VI (1998) Thermomechanical Theory of Martensitic Phase Transformations in Inelastic Materials. *Int. J. Solids and Structures* 35: 889-940.

[2] Levitas VI (2000) Structural Changes Without Stable Intermediate State in Inelastic Material. Parts I and II. *Int. J. Plasticity* 16: 805-849 and 851-892.

[3] Lomdahl PS, Tamayo P, Grnbech-Jensen N and Beazley DM (1993), *Proceedings of Supercomputing 93*, G. S. Ansell, Ed. (IEEE Computer Society Press, Los Alamitos, CA), 520527.

[4] Holian BL and Lomdahl PS (1998) Plasticity induced by shock waves in nonequilibrium molecular-dynamics simulations. *Science* 80: 2085-2088.

[5] Ravelo R, Holian BL, Germann TC, Lomdahl PS (2004) Constant-Stress Hugoniostat Method for Following the Dynamical Evolution of Shocked Matter. *Phys. Rev B* 70: 014103.

[6] Ravelo R, Holian BL and Germann TC (2009) High Strain Rates Effects in Quasi-Isentropic Compression of Solids. *AIP Conf. Proc.* 1195: 825-830.

[7] Mishin Y et al. (2001) Structural Stability and Lattice Defects in Copper: Ab Initio, Tight-Binding, and Embedded-Atom Calculations. *Phys. Rev. B* 63: 224106.

[8] Angelo JE, Moody NR and Baskes MI (1995) Trapping of Hydrogen to Lattice-Defects in Nickel. *Model. Simul. Mater. Sci. Eng.* 3: 289-307.

[9] Ten Wolde PR, Ruiz-Montero MJ, and Frankel D (1995) Numerical Evidence for bcc Ordering at the Surface of a Critical fcc Nucleus. *Phys. Rev. Lett.* 75: 2714-2717.

[10] Steinhardt PJ, Nelson DR, and Ronchetti M (1983) Bond-Orientational Order in Liquids and Glasses. *Phys. Rev. B* 28: 784-805.